On the Dual-Rod Slider Rocker Mechanism and Its Applications to Tristate Rigid Active Docking

Paul M. Moubarak
e-mail: paul4@gwu.edu

Pinhas Ben-Tzvi[1]
e-mail: bentzvi@gwu.edu

Robotics and Mechatronics Laboratory,
The George Washington University,
Washington, DC 20052

The dual-rod slider rocker mechanism is equivalent to two traditional single-rod sliders that share a common rocker, where the sliders translate along two opposite directions. Unlike a single-rod system, the dual-rod mechanism is unique, in the sense that the two sliders do not translate the same distance for the same rocker rotation. In this paper, an optimal kinematic and dynamic analysis of the dual-rod slider rocker mechanism is presented. This analysis is supplemented by an application to modular robotic coupling, in which the mechanism is employed by a torque recirculation scheme to enable three independent modes of operation via a single motor. Simulation, finite element analysis, and experimental results validate the kinematic properties of this mechanism, the rigidity of the proposed docking interface, and its three modes of operation. We conclude that the compactness of the dual-rod mechanism, and its unique kinematic properties, exhibits a broad industrial value for applications where size and weight are a critical design constraint, such as space and mobile robotics. [DOI: 10.1115/1.4023178]

Keywords: dual-rod slider rocker mechanism, kinematic analysis, dynamics, multi-objective optimization, rigid active docking, finite element analysis

1 Introduction

In today's industry, the single-rod slider crank or rocker mechanism largely dominates applications where a rotary motion is converted into a translation, or vice versa. The most common example of these applications is in the automotive industry, where the single-rod slider-crank mechanism represents a fundamental component of internal combustion engine technology [1]. In contrast, the industrial applications of the dual-rod slider rocker mechanism, which represent an interesting variation of the single-rod system, remain unexplored.

From a structural perspective, the dual-rod mechanism consists of two symmetric single-rod sliders that share a common rocker, where the translation of the sliders occurs in opposite directions. As will be shown in this paper, the kinematic properties of this assembly are unique, in the sense that the two sliders do not travel the same distance for the same rocker rotation. This means that the time-dependant position of one slider will, at all times, either lead or lag the position of the other slider throughout the combined stroke.

Traditionally, the broad industrial applications of the single-rod slider system motivated a continual research effort to understand its kinematic and dynamic properties [2–9], even for less common variations of the traditional design [10,11] with flexible rods [12–15] or spatial slider trajectories [16–19]. In contrast, and to the best knowledge of the authors, no work has been reported on the kinematic and dynamic characteristics of the dual-rod system due to its limited industrial applications.

Nonetheless, with the recent developments in space applications and mobile robotic technology, there has been a greater demand for new mechanisms that are either compact, or enable the initiation of multiple tasks via a single actuator, or sometimes even both. This trend is driven by the continual desire to develop mechanical systems (such as mobile robots) that deliver maximum power with the smallest and lightest assembly possible.

The dual-rod slider rocker mechanism stands out as one of these systems that can have significant applications in space and robotic technology, where a rotary motion of a single actuator is converted into a translation of multiple sliders. The main advantage of this mechanism is attributed to its minimal footprint. This footprint is considerably smaller than other mechanical systems that enable the translation of multiple sliders via a single motor, such as the leadscrew mechanism [20,21].

In this paper, the kinematic and dynamic properties of the dual-rod slider rocker mechanism are introduced. Because the sliders of this system translate at two different rates for the same rocker rotation, a multi-objective optimality analysis is formulated. The solution of this analysis generates optimal rod dimensions that enable the sliders to meet terminal spatial boundary conditions (BC). Indeed, because of this relative displacement offset, the dual-rod system is mostly relevant to applications where the sliders' translation is constrained to meet terminal boundary conditions at the same time, while tolerating minimal relative displacement offset in the intermediate stroke. A potential embodiment of these applications is sliding doors, where two doors driven by a single actuator are simultaneously required to meet the *open* and *close* boundary conditions, irrespective of any relative translation offset that may exist in the intermediate stroke.

The sample robotic application proposed in this paper for the dual-rod slider rocker mechanism is docking interfaces for modular robotics. In fact, a recent research trend in the field of mobile robotics has seen an increased interest in reconfigurable robots [22–24] due to their small individual size, and their projected adaptive mobility and manipulation capabilities on rough terrain. The main merit of the proposed coupling interface lies in its ability to provide structural non-back-drivability for high-payload active docking applications, while maintaining a compact assembly by recirculating motor torque to accomplish three tasks via a single motor.

This torque recirculation scheme is enabled by a dual-rod slider rocker mechanism, which allows the interface to operate in three independent modes. In the *drive mode*, the interface drives the module. In the *clamp mode*, the interface enables the module to rotate relative to its neighbors in the formation. In the *neutral mode*, the motor torque aligns the mating elements prior to docking. The design details of this interface are presented in this paper,

[1]Corresponding author.

Contributed by the Mechanisms and Robotics Committee of ASME for publication in the Journal of Mechanisms and Robotics. Manuscript received May 3, 2012; final manuscript received November 25, 2012; published online January 24, 2013. Assoc. Editor: Anupam Saxena.

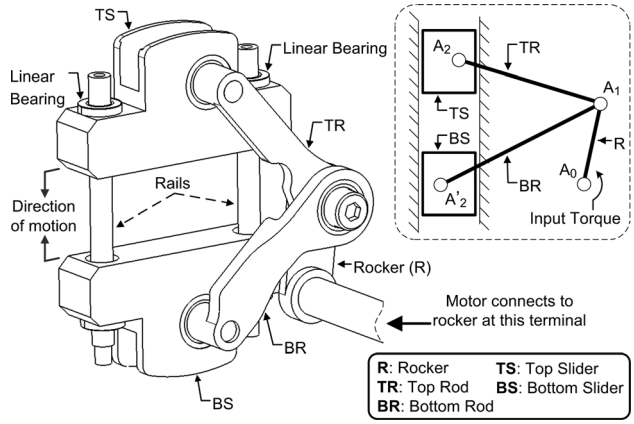

Fig. 1 Isometric schematic and corresponding kinematic diagram of the dual-rod slider rocker mechanism

along with a finite element force analysis that validates its structural non-back-drivability. Simulation and experimental results further demonstrate the kinematic properties of the dual-rod mechanism, and the interface's proposed modes of operation.

2 Kinematics of the Dual-Rod Slider Rocker Mechanism

A schematic of the dual-rod slider rocker mechanism and its kinematics are depicted in Figs. 1 and 2, respectively. The top and bottom rods connect a single rocker, driven by a single actuator, to two sliders which translate along two parallel rails, guided by linear bearings, where the top slider moves in the opposite direction of the bottom slider.

Because the motion of the sliders is constrained to a pure translation along the rails, the kinematic dependency between the rocker's angle and the top and bottom rod angles can be expressed in terms of θ_1 as

$$\sin(\theta_2) = \frac{l_1 \sin(\theta_1) + b}{l_2} \tag{1}$$

$$\sin(\theta'_2) = \sin(\pi - \theta'_2) = \frac{l_1 \sin(\theta_1) + b'}{l'_2} \tag{2}$$

These equations enable the derivation of two expressions for the translation of the top and bottom sliders as a function of θ_1. These can be written for the top slider as

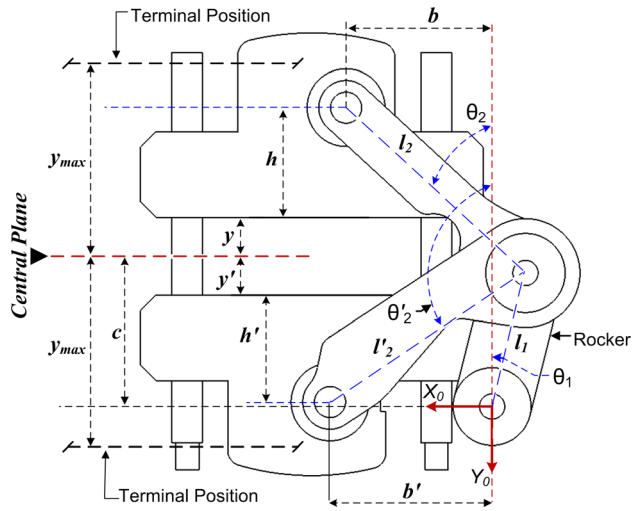

Fig. 2 Kinematics of the dual-rod slider rocker mechanism

$$y = l_1 \cos(\theta_1) + l_2 \sqrt{1 - \left\{ \frac{l_1 \sin(\theta_1) + b}{l_2} \right\}^2} - c - h \tag{3}$$

and for the bottom slider as

$$y' = l_1 \cos(\theta_1) - l'_2 \sqrt{1 - \left\{ \frac{l_1 \sin(\theta_1) + b'}{l'_2} \right\}^2} - c + h' \tag{4}$$

where based on the reference frame X_0Y_0, $y > 0$ and $y' < 0$.

From Eqs. (3) and (4), it is obvious that the displacement difference between the top and the bottom sliders, defined as $e = y + y'$, is not equal to zero $\forall\theta_1$, even if the two single-rod slider rocker mechanisms were designed symmetrically with respect to the central plane. In such case, if b', l'_2, and h' were chosen equal to b, l_2, and$h$, respectively, the offset e becomes

$$e = 2l_1 \cos(\theta_1) - 2c \neq 0 \ \forall\theta_1 \tag{5}$$

which represents an explicit function of θ_1 that is not equal to zero $\forall\theta_1$. This infers that the two sliders do not travel the same distance for the same rocker rotation.

3 Optimal Kinematic Analysis

In this section, an optimal analysis for the generic design of the dual-rod slider rocker mechanism is presented. In general, the offset e resulting from the kinematic properties of the dual-rod mechanism dictates applications where the two sliders are constrained to meet terminal BC at the same time, while tolerating minimal relative displacement offset in the intermediate stroke. For these boundary conditions to be met, the dimensions of the mechanism's rods should be derived as a solution to the optimal problem $e = 0|_{BC}$.

At first, a general expression for e can be written in terms of the 12 parameters that define the dual-rod slider rocker mechanism, as illustrated in Fig. 2

$$e = f(\theta_1, b, l_1, l_2, b', l'_2, h, h', c, \theta_{1,y_0}, \theta_{1,y\max}, y_{\max}) \tag{6}$$

This expression can be subsequently reduced by considering the geometric constraints and the kinematic dependencies that exist between the different parameters in (6). For this, one should first select a single-rod slider rocker mechanism as a reference for ensuing optimality analysis.

If the top rod/slider assembly is selected as a reference, the first objective will be to increase the force transmission efficiency by maximizing the push/pull (Y_0-axis) component of the force transmitted to the top slider via the top rod. This can be accomplished by choosing the smallest value of b and the largest value of h that the top slider's dimensions can accommodate.

Similarly, the rocker parameters $c, l_1,$ andθ_{1,y_0} can be selected to meet other geometric constraints imposed by the mechanism design. For instance, one can chose a combination $(c, l_1, \theta_{1,y0})$ that prevents the rocker angle from exceeding a certain threshold imposed by the design, such as preventing the tip of the rocker from interfering with the frame of the mechanism at $y = y' = 0$ (an example of such consideration will be given in Sec. 6.2.3). These selected parameters enable the calculation of an analytical expression for l_2 as

$$l_2^2 = l_1^2 + b^2 + (c+h)^2 - 2l_1\sqrt{b^2 + (c+h)^2}\cos\left(\theta_{1,y_0} + tg^{-1}\left\{\frac{b}{c+h}\right\}\right) \tag{7}$$

which enables the derivation of an implicit quadratic equation in $\theta_{1,y_{\max}}$ as

$$p\cos(\theta_{1,y_{\max}}) - b\sin(\theta_{1,y_{\max}}) = \frac{p^2 + l_1^2 - l_2^2 + b^2}{2l_1} \triangleq \rho \tag{8}$$

whose solution generates an analytical expression for $\theta_{1,y_{\max}}$

$$\theta_{1,y_{\max}}^{1,2} = \sin^{-1}\left(\frac{-\rho b \pm p\sqrt{p^2 - \rho^2 + b^2}}{b^2 + p^2}\right) \tag{9}$$

where in (9), $p = c + h + y_{\max}$. The two solutions in (9) correspond to the *elbow up* and *elbow down* configurations of the top rocker/rod assembly. Typically however, in the presence of terminal *open* boundary conditions, only the *elbow up* solution ($\theta_{1,y_{\max}}^{1}$) will be feasible since the translation of the sliders will be restrained to a maximum stroke threshold defined by $y_{\max}$, thus preventing the *elbow down* configuration from occurring. As such, $y_{\max}$ represents another design parameter that is selected to define the stroke length of the top and bottom sliders as dictated by the mechanism's application.

With these selected values, the offset expression will be reduced to $e = f(\theta_1, b', l_2', h')$. However, since e remains a direct function of θ_1, there exist no unique values for (b', h', l_2') that meet the condition $e = 0 \forall \theta_1$. Nonetheless, the error e can be minimized at the boundaries to generate optimal dimensions for the bottom rod which enable the sliders to simultaneously meet the *open* and *close* boundary conditions.

The consideration of the *close* BC $y' = 0|_{\theta_{1,y_0}}$ enables the derivation of an analytical expression for l_2' as

$$l_2'^2 = l_1^2 + b'^2 + (c - h')^2 - 2l_1\sqrt{b'^2 + (c - h')^2}\cos\left(tg^{-1}\left\{\frac{b'}{c - h'}\right\} + \theta_{1,y_0}\right) \tag{10}$$

which guarantees the nonviolation of the *close* (central plane) boundary condition $\forall b', h'$. The substitution of (10) into (4), and (7) into (3) yields a final expression for e as

$$e(\theta_1, b', h') = 2l_1\cos(\theta_1) + \sqrt{l_2^2 - (l_1\sin(\theta_1) + b)^2} - 2c - h + h' - \sqrt{b'^2 + (c - h')^2 + l_1^2 - \left(2\sqrt{b'^2 + (c - h')^2}\right)\left(l_1\cos\left\{\theta_{1,y_0} + tg^{-1}\left(\frac{b'}{c - h'}\right)\right\}\right) - (l_1\sin(\theta_1) + b')^2} \tag{11}$$

which can be minimized to calculate the optimal pair $(b', h')^{\text{opt}}$ that enables the dual-rod mechanism to meet the *open* boundary condition $y' = y_{\max}|_{\theta_{1,y_{\max}}}$.

However, the cost function defined in (11) alone is not enough. In fact, similar to the choice of b and h, the optimal pair $(b', h')^{\text{opt}}$ should also maximize the force transmission efficiency of the bottom slider rocker mechanism defined by the cost function

$$\zeta(\theta_1, b', h') = \sqrt{1 - \left(\frac{l_1\sin(\theta_1) + b'}{l_2'}\right)^2} = \frac{({}^0F_{\text{Brod}})_{Y_0}}{{}^0F_{\text{Brod}}} \tag{12}$$

where ${}^0F_{\text{Brod}}$ defines the force transmitted by the bottom rod and expressed in the reference frame X_0Y_0, and $({}^0F_{\text{Brod}})_{Y_0}$ the component of ${}^0F_{\text{Brod}}$ along the Y_0-axis.

Moreover, because the error e is left unbounded in the intermediate stroke, one should also cap the supremum of the set $e(\theta_1, b', h')$ to an acceptable threshold δ whose value represents a design compromise between the maximum allowable offset e and the minimum acceptable efficiency ζ. This consideration, along with the two cost functions defined in (11) and (12), can be aggregated into a multi-objective optimization problem stated as follows:

$$\begin{aligned} &\underset{b',h' \in \Omega}{\text{Min}} \quad |e(\theta_1, b', h')|_{\theta_{1,y_{\max}}} \\ &\underset{b',h' \in \Omega}{\text{Max}} \quad \zeta(\theta_1, b', h')|_{\theta_{1,y_{\max}}} \\ &\text{subject to} \quad \sup|e(\theta_1, b', h')| < \delta \\ &\text{and the set of geometric constraints } \Omega = \begin{cases} b'_{\min} \le b' \le b'_{\max} \\ h'_{\min} \le h' \le h'_{\max} \end{cases} \end{aligned} \tag{13}$$

where $b'_{\min}$, $b'_{\max}$, $h'_{\min}$, and $h'_{\max}$ determine the geometric range of allowable values of b' and h' as dictated by the desired dimensions of the bottom slider. Those geometric constraints ensure that the optimal solution of (13) corresponds to a rod/slider joint location that is contained in the X_0Y_0 cross-section of the slider (i.e., that the rod-slider joint is not outside the slider). In (13), $|e(\theta_1, b', h')|$ denotes the absolute value of e since the displacement offset could fluctuate between a positive and a negative threshold.

4 Optimal Solution: A Case-Study

The optimality problem formulated in (13) can be resolved deterministically if one cost function is converted into an inequality constraint. The choice for this candidate function is based on a priority decision that takes into account the physical connotations of the solution. That is, since it is a design requirement to ensure that $e = 0$ at $\theta_{1,y_{\max}}$, then maintaining $e < \varepsilon$ at $\theta_{1,y_{\max}} (\varepsilon \ll 1)$ takes priority over maximizing $\zeta(\%)$ at $\theta_{1,y_{\max}}$ to above a minimum threshold. The alternative approach where the multi-objective problem is either solved as a set of Pareto optimal points [25], or where the objective is to maintain $\zeta > \zeta_{\min}$ causes the optimal solution to minimize the offset e to an unspecified threshold. This threshold is not necessarily near zero, which in such case will cause the solution to violate the *open* terminal boundary condition.

Therefore, by converting $e(\theta_1, b', h')$ to an inequality constraint, a full control over the magnitude of e at the boundary is given through the value of ε, and the optimality problem in (13) can be restated as

$$\begin{aligned} &\underset{b',h' \in \Omega}{\text{Max}} \quad \zeta(\theta_1, b', h')|_{\theta_{1,y_{\max}}} \\ &\text{subject to} \quad g(\theta_1, b', h') = \begin{cases} |e(\theta_1, b', h')|)_{\theta_{1,y_{\max}}} < \varepsilon \\ \sup|e(\theta_1, b', h')| < \delta \end{cases} \\ &\text{and the set of geometric constraints } \Omega = \begin{cases} b'_{\min} \le b' \le b'_{\max} \\ h'_{\min} \le h' \le h'_{\max} \end{cases} \end{aligned} \tag{14}$$

A case-study solution for (14) is shown in Fig. 3, for $18.5 \le b' \le 26.5$ and $10.5 \le h' \le 14.4$, with $b = 18.1$ mm, $h = 14.1$ mm, $c = 19$ mm, $l_1 = 17.7$ mm, $\theta_{1,y_0} = 27$ deg, $\theta_{1,y_{\max}} = -4.05$ deg, $y_{\max} = 11$mm, and $\delta = 0.6$ mm. This solution space S is visualized as part of a meshed space Λ ($S \subset \Lambda$, where Λ is the meshed space of Ω) of three subsets, where the optimal subset containing all pairs (b', h') that meet the constraints $g(\theta_1, b', h')$ is cascaded between an upper and a lower subset containing the pairs (b', h') that meet *at best* one constraint in g.

The difference between the upper and the lower subsets is in the magnitude of the efficiency ζ. The lower subset delivers efficiencies that are either lower or comparable to those corresponding to the optimal subset. The upper subset generates efficiencies that are comparable or higher than the efficiencies of the optimal subset. However, because such higher efficiency comes at the expense of the constraints which are violated in the upper subset,

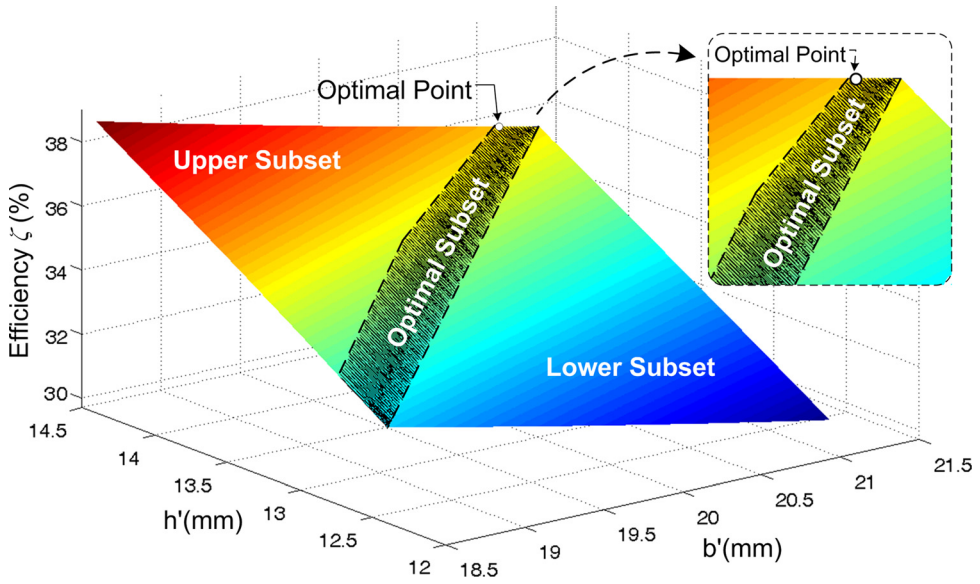

Fig. 3 Meshed solution space of the optimal problem in (14)

the optimal pair $(b', h')^{\text{opt}}$ that maximizes the efficiency without violating any constraints is selected near the top edge of the optimal subset at $b' = 21.02$mm, $h' = 14.39$mm, with $\zeta = 35.5\%$ for the selected case-study (Fig. 3). We note that the boundaries defining the optimal subset are inclusive of this subset.

5 Dynamics of the Dual-Rod Slider Rocker Mechanism

The dynamic formulation of the dual-rod slider rocker mechanism is outlined in this section to validate the feasibility of the optimality analysis presented in Secs. 3 and 4. That is, for a given torque or velocity input to the rocker, a solution of the equations of motion is derived to demonstrate the ability of the mechanism to simultaneously reach the terminal boundary conditions in the upward and downward strokes, while capping the relative displacement offset to the specified threshold δ in the intermediate stroke.

5.1 Equations of Motion. The free body diagram of the dual-rod slider rocker mechanism is as shown in Fig. 4. Based on this diagram, the conservation of the rocker's linear and angular momentum generates the following dynamic equations of motion:

$$\begin{aligned} &F_{x_0} + F_{x_1} + F'_{x_1} = {M_1}^0 \ddot{x}_{G_1} \\ &F_{y_0} + F_{y_1} - F'_{y_1} = {M_1}^0 \ddot{y}_{G_1} \\ &-\left(F_{x_1} + F'_{x_1}\right) l_1 \cos\theta_1 - \left(F_{y_1} - F'_{y_1}\right) l_1 \sin\theta_1 + \tau = {J_{A_0}}^0 \ddot{\theta}_1 \end{aligned} \tag{15}$$

where $F_{x_0}, F_{y_0}, F_{x_1}, F_{y_1}, F'_{x_1}$, and F'_{y_1} are external forces acting on the rocker and the rods, and expressed in the global frame of reference (Fig. 4). J_{A_0} defines the polar moment of inertia of the rocker relative to its joint, τ the torque acting on the rocker, and $(\ddot{x}_{G_1}, \ddot{y}_{G_1})$ the acceleration components of the rocker's center of gravity relative to the global frame.

Similarly, the conservation of linear and angular momentum applied to the top and bottom rods, respectively, generates equations of motion for the top rod of the form

$$\begin{aligned} &F_{x_2} - F_{x_1} = {M_2}^0 \ddot{x}_{G_2} \\ &F_{y_2} - F_{y_1} = {M_2}^0 \ddot{y}_{G_2} \\ &F_{x_2}\left(l_2 - l_{_{G_2}}\right)\cos\theta_2 - F_{y_2}\left(l_2 - l_{_{G_2}}\right)\sin\theta_2 \\ &+ F_{x_1} l_{_{G_2}} \cos\theta_2 - F_{y_1} l_{_{G_2}} \sin\theta_2 = J^0_{G_2} \ddot{\theta}_2 \end{aligned} \tag{16}$$

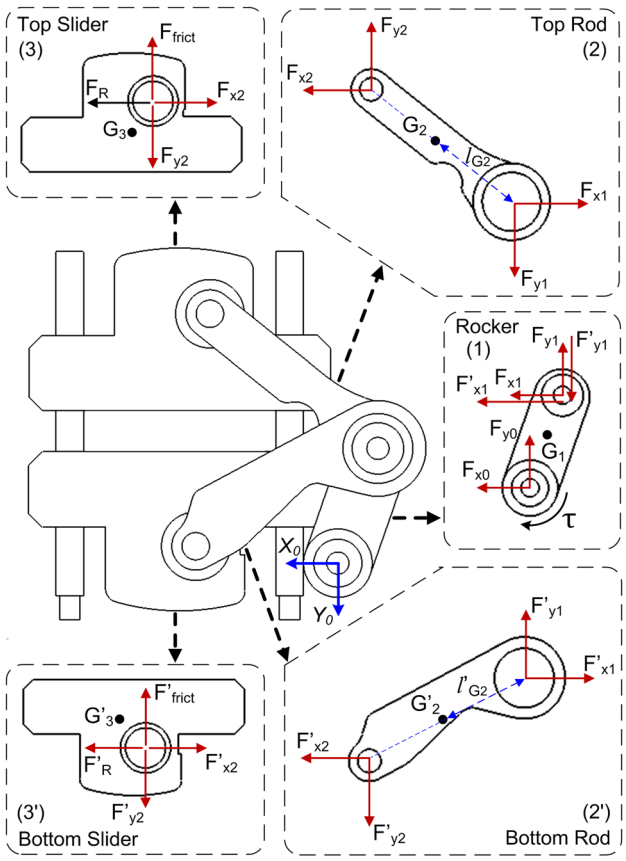

Fig. 4 Free body diagram of the dual-rod slider rocker mechanism

and for the bottom rod of the form

$$\begin{aligned} &F'_{x_2} - F'_{x_1} = {M'_2}^0 \ddot{x}_{G'_2} \\ &-F'_{y_2} + F'_{y_1} = {M'_2}^0 \ddot{y}_{G'_2} \\ &F'_{x_1} l'_{G2} \cos\theta'_2 + F'_{x_2}\left(l'_2 - l'_{G2}\right)\cos\theta'_2 \\ &+ F'_{y_1} l'_{G2} \sin\theta'_2 + F'_{y_2}\left(l'_2 - l'_{G2}\right)\sin\theta'_2 = {J_{G'_2}}^0 \ddot{\theta}'_2 \end{aligned} \tag{17}$$

In these equations, F_{x_2}, F_{y_2}, F'_{x_2}, and F'_{y_2} define the external forces acting on the top and bottom rods, respectively, as shown in Fig. 4, J_{G_2} and $J_{G'_2}$ the polar moments of inertia of the top and bottom rods relative to their respective centers of gravity, and $(\ddot{x}_{G_2}, \ddot{y}_{G_2}, \ddot{x}_{G'_2}, \ddot{y}_{G'_2})$ the acceleration components of the center of gravity of the top and bottom rods relative to the global frame. l_{G_2} and l'_{G_2} define the distance separating the center of mass of the top and bottom rods from their joint axes, respectively (Fig. 4).

For the sliders on the other hand, the dynamic motion is constrained to a translation along the rails, which simplifies the equations of motion for the top slider to

$$\begin{aligned} F_R - F_{x_2} &= 0 \\ F_{\text{frict}} - F_{y_2} &= M_3 {}^0\ddot{y}_{G_3} \end{aligned} \tag{18}$$

and for the bottom slider to

$$\begin{aligned} F'_R - F'_{x_2} &= 0 \\ F'_{y_2} - F'_{\text{frict}} &= M'_3 {}^0\ddot{y}_{G'_3} \end{aligned} \tag{19}$$

where F_R and F'_R are the reaction forces,F_{frict} and F'_{frict} are the sliding friction forces acting on the top and bottom sliders, respectively. $(\ddot{y}_{G_3}, \ddot{y}_{G'_3})$ represent the acceleration components of the center of gravity of the top and bottom sliders relative to the global frame. These acceleration components, along with the accelerations of the rocker and the rods, can be expressed explicitly in terms of $\theta_1, \theta_2, \theta'_2$ and their first and second order derivatives, as follows:

$$\begin{aligned} {}^0\ddot{x}_{G_1} &= l_{G_1}\dot{\theta}_1^2 \sin\theta_1 - l_{G_1}\ddot{\theta}_1 \cos\theta_1 \\ {}^0\ddot{y}_{G_1} &= -l_{G_1}\dot{\theta}_1^2 \cos\theta_1 - l_{G_1}\ddot{\theta}_1 \sin\theta_1 \end{aligned} \tag{20}$$

$$\begin{aligned} {}^0\ddot{x}_{G_2} &= -l_1\ddot{\theta}_1 \cos\theta_1 + l_1\dot{\theta}_1^2 \sin\theta_1 + l_{G_2}\ddot{\theta}_2 \cos\theta_2 - l_{G_2}\dot{\theta}_2^2 \sin\theta_2 \\ {}^0\ddot{y}_{G_2} &= -l_1\ddot{\theta}_1 \sin\theta_1 - l_1\dot{\theta}_1^2 \cos\theta_1 - l_{G_2}\ddot{\theta}_2 \sin\theta_2 - l_{G_2}\dot{\theta}_2^2 \cos\theta_2 \end{aligned} \tag{21}$$

$$\begin{aligned} {}^0\ddot{x}_{G'_2} &= -l_1\ddot{\theta}_1 \cos\theta_1 + l_1\dot{\theta}_1^2 \sin\theta_1 + l'_{G_2}\ddot{\theta}'_2 \cos\theta'_2 - l'_{G_2}\dot{\theta}'^2_2 \sin\theta'_2 \\ {}^0\ddot{y}_{G'_2} &= -l_1\ddot{\theta}_1 \sin\theta_1 - l_1\dot{\theta}_1^2 \cos\theta_1 - l'_{G_2}\ddot{\theta}'_2 \sin\theta'_2 - l'_{G_2}\dot{\theta}'^2_2 \cos\theta'_2 \end{aligned} \tag{22}$$

$$\begin{aligned} {}^0\ddot{x}_{G_3} &= -l_1\ddot{\theta}_1 \cos\theta_1 + l_1\dot{\theta}_1^2 \sin\theta_1 + l_2\ddot{\theta}_2 \cos\theta_2 - l_2\dot{\theta}_2^2 \sin\theta_2 = 0 \\ {}^0\ddot{y}_{G_3} &= -l_1\ddot{\theta}_1 \sin\theta_1 - l_1\dot{\theta}_1^2 \cos\theta_1 - l'_2\ddot{\theta}_2 \sin\theta_2 - l_2\dot{\theta}_2^2 \cos\theta_2 \end{aligned} \tag{23}$$

$$\begin{aligned} {}^0\ddot{x}_{G'_3} &= -l_1\ddot{\theta}_1 \cos\theta_1 + l_1\dot{\theta}_1^2 \sin\theta_1 + l'_2\ddot{\theta}'_2 \cos\theta'_2 - l'_2\dot{\theta}'^2_2 \sin\theta'_2 = 0 \\ {}^0\ddot{y}_{G'_3} &= -l_1\ddot{\theta}_1 \sin\theta_1 - l_1\dot{\theta}_1^2 \cos\theta_1 - l'_2\ddot{\theta}'_2 \sin\theta'_2 - l'_2\dot{\theta}'^2_2 \cos\theta'_2 \end{aligned} \tag{24}$$

The equations of motion (15)–(19), and the acceleration kinematics in (20)–(24), can be further aggregated in a matrix format [26] of the following form:

$$\begin{aligned} &[\boldsymbol{C_F}(\theta)]^{23\times 120} F_{ext} + [\boldsymbol{D}_\tau]^{23\times 10} \tau_{ext} + [\boldsymbol{V}(\theta)]^{23\times 20} \dot{\omega} \\ &\quad - [\boldsymbol{M}]^{23\times 80} a = \left[\boldsymbol{C}_\omega(\theta, \dot{\theta})\right]^{23\times 1} \end{aligned} \tag{25}$$

where ${}^0\dot{\omega} = \begin{bmatrix} {}^0\ddot{\theta}_2 & {}^0\ddot{\theta}'_2 \end{bmatrix}^T$. In (25), $\boldsymbol{C_F}(\theta)$ and $\boldsymbol{D}_\tau$ define the matrix coefficients of external forces ${}^0F_{\text{ext}}$ and external torques ${}^0\tau_{\text{ext}}$, respectively, $\boldsymbol{V}(\theta)$ the matrix coefficient of angular accelerations of the top/bottom rods, $\boldsymbol{M}$ the mass matrix, and $\boldsymbol{C}_\omega(\theta, \dot{\theta})$ the input vector including the rocker's angular velocity.

5.2 Dynamic Simulation: A Case-Study. A case-study solution of (25) is derived to validate the optimal analysis of the dual-rod slider rocker mechanism, and the fact that the optimal rod dimensions do enable the two sliders to simultaneously reach a given terminal boundary condition, despite the relative displacement offset that exists in the intermediate stroke. In this simulation, the rocker is driven at a sample constant angular velocity ${}^0\dot{\theta}_1 = 15\,\text{deg/s}$, with a coefficient of static friction $\mu_s = 0.29$ applied to the sliding motion of the sliders along the rails (steel on steel). Furthermore, the dimensions, masses, and polar moments of inertia employed in this simulation are as summarized in Table 1. These values are extracted from the computer aided design model of the mechanism's parts corresponding to the prototype application presented later in Sec. 6.

Table 1 Summary of dimensions, masses, and polar moments of inertia for the five links of the dual-rod slider rocker mechanism in both the case-study dynamic simulation and the proof-of-concept prototype of Fig. 9

Link	Length (mm)	Location of COG (mm)	Polar inertia ($\text{g} \times \text{mm}^2$)	Mass (g)
Rocker	$l_1 = 17.7$	$l_{G_1} = 7.48$	$J_{A_0} = 699$	$M_1 = 6.5$
Top rod	$l_2 = 31.35$	$l_{G_2} = 14.53$	$J_{G_2} = 964$	$M_2 = 6.05$
Bottom rod	$l'_2 = 30.1$	$l_{G'_2} = 14.95$	$J_{G'_2} = 1177$	$M'_2 = 9.1$
Top slider	N/A	N/A	N/A	$M_3 = 11.55$
Bottom slider	N/A	N/A	N/A	$M'_3 = 11.26$

The simulation of the scenario where the sliders are driven down from the *open* to the *close* terminal boundary is visualized in Fig. 5. In this figure, it is shown that the dimensions of the rods resulting from the optimality problem in (14) enable the two sliders to reach the *close* boundary condition (the central plane) at the same time after ~2.1 s. This interception at the central plane happens, despite the relative translation offset that exists between the two sliders as further highlighted in Fig. 5.

Because of this offset, the two sliders move and accelerate at two different rates—albeit driven by the same motor—in order to reach the same terminal position at the same time. This is shown in Figs. 6 and 7, where the sliders' velocity and acceleration profiles are plotted as a function of time.

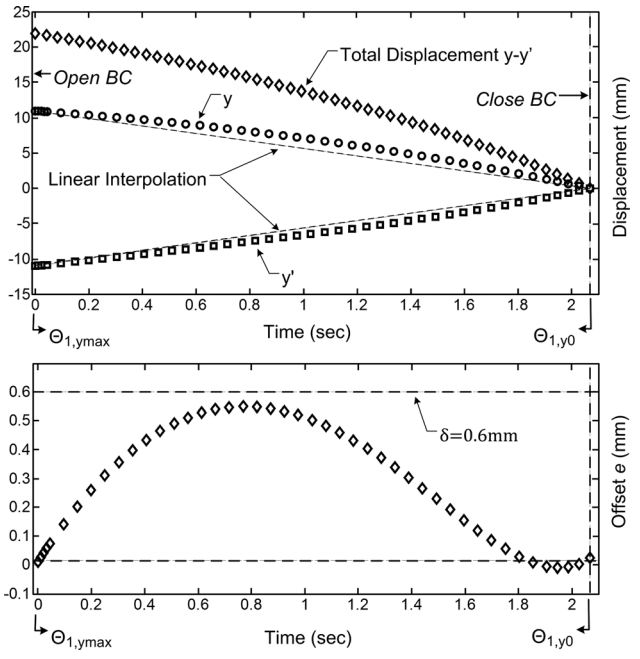

Fig. 5 Displacements of top slider (y), bottom slider (y'), combined stroke ($y - y'$), and relative translation offset plotted versus time

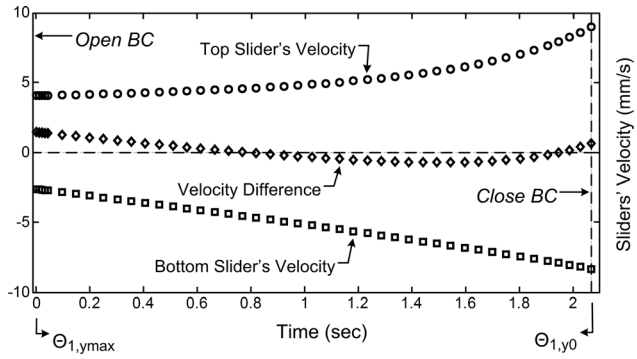

Fig. 6 Velocity profiles of the top and bottom sliders, and relative velocity difference, plotted as a function of time for $\dot{\theta}_1 = 15°/s$

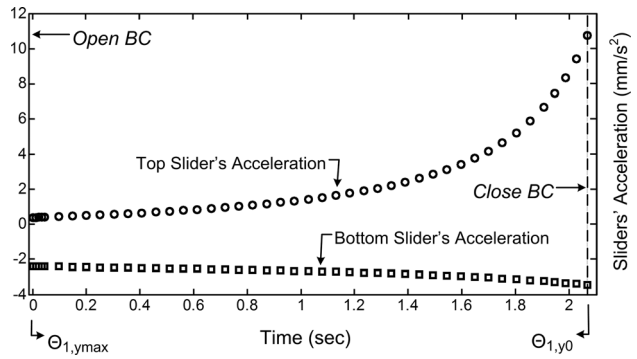

Fig. 7 Acceleration profiles of the top and bottom sliders, plotted as a function of time for $\dot{\theta}_1 = 15°/s$

In Fig. 6 in particular, it is noted that the sliders alternate the leading velocity in the intermediate stroke. This is depicted by the profile of the velocity difference which fluctuates between a positive and a negative threshold. Moreover, this simulation proves that the offset e remains capped to the threshold δ, which complies with (14), and further validates the optimality analysis derived in Sec. 3.6.

6 Case-Study Application: Docking Interface

A robotic application of the dual-rod slider rocker mechanism is proposed in this section. This application relates to docking interfaces for modular robotics, where the dual-rod mechanism is integrated in a torque recirculation scheme that enables three independent tasks via a single *high-torque* motor. The configuration of the dual-rod mechanism further ensures the rigidity, reversibility, and non-back-drivability of the interface as will be discussed in Sec. 6.4. These attributes, which cannot be provided by existing magnetic [27–29] or shape memory alloy (SMA)-actuated coupling interfaces [30–32], represent an essential component for modular robotic mobility and manipulation on rough terrain.

6.1 Tristate Docking Interface: Design Overview. The proposed coupling interface enables docking between two adjacent modules in a chain architecture [23]. In this chain, the male part of the interface (or the *T-Mech: Translational Mechanism* (Fig. 8)) consists of a translational docking shaft driven by a rack and pinion mechanism and is carried by one module. The female part (or the *C-Mech: Clamping Mechanism* (Fig. 9)) consists of a clamping system driven by a dual-rod slider rocker mechanism, and is carried by another module in the formation. A simplified schematic of this interface is shown in Fig. 8, and an animation of the

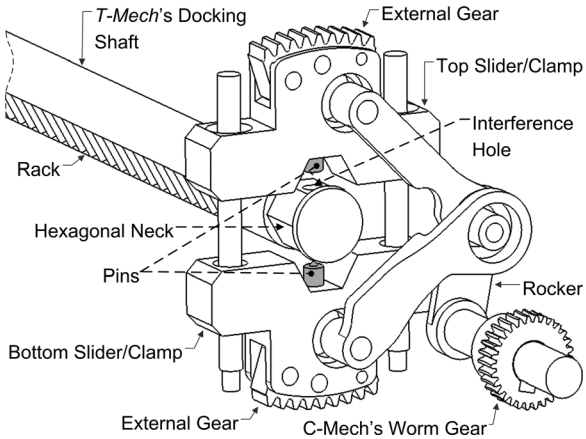

Fig. 8 Schematic of the coupling interface showing the docking shaft and the dual-rod slider rocker mechanism

docking process for a sample three-module formation can be found in Ref. [33].

The sliders of the dual-rod mechanism act as the clamps for this docking system, and further carry external gear segments that engage an internal gear carried by a coupler. In fact, the entire dual-rod system fits inside a rectangular frame which in turn fits inside the coupler, as shown in Fig. 9. This rectangular frame is rigidly connected to a hollow main shaft which is driven by a central *high-torque* motor via a central worm and worm gear assembly. The coupler on the other hand is rigidly connected to the driving system of the module. For instance, in Fig. 9, the coupler is shown connected to the drive pulley of a small mobile robot.

The hollow main shaft enables the insertion of the docking shaft toward the clamps until it is stopped by an appendix, best shown in the transmission schematic of the interface in Fig. 10. This shaft carries a hexagonal neck with interference holes which mate with protruded pins (Fig. 8) carried by the corresponding hexagonal aperture of the clamps. The location of the appendix inside the *C-Mech* is defined in a way to cause the plane of the pins to coincide with the plane of the holes when the shaft hits the appendix. In such case, the alignment between the pins and the holes will be reduced to a re-orientation of the sliders around the docking shaft in the *neutral mode*.

The rocker that drives these clamps is actuated by a low-torque selection motor via the *C-Mech*'s worm and worm gear assembly which ensures the mechanical non-back-drivability of the sliders. Power to the selection motor, the linear encoder that measures the combined displacement of the sliders, and the *C-Mech*'s electronics is provided by the modules' battery. However, because of the relative rotary motion between the *C-Mech* and the frame of the module, two pairs of graphite brushes are integrated in the assembly to create permanent spring-loaded contact with isolated copper rims on two PCB boards. These two PCBs (PCB-F and PCB-C), best shown in Fig. 10, funnel the current from the battery to the *C-Mech*'s electrical components. Motor command and sensor data are also communicated between the *C-Mech* and the module over a wireless grid established with two X-Bee modules (2.4 GHz), which enable the endless rotation of the *C-Mech* inside the coupler.

6.2 Modes of Operation. The dual-rod slider rocker mechanism, integrated as part of the docking interface, initiates a torque recirculation scheme which enables the interface to operate in three independent modes: *drive*, *neutral*, and *clamp*.

6.2.1 Drive Mode. In the *drive mode*, the sliders are moved in the outward direction until the two external gear segments engage the internal gear of the coupler as shown in Figs. 9–11(*a*). This mode corresponds to the *open* terminal boundary condition

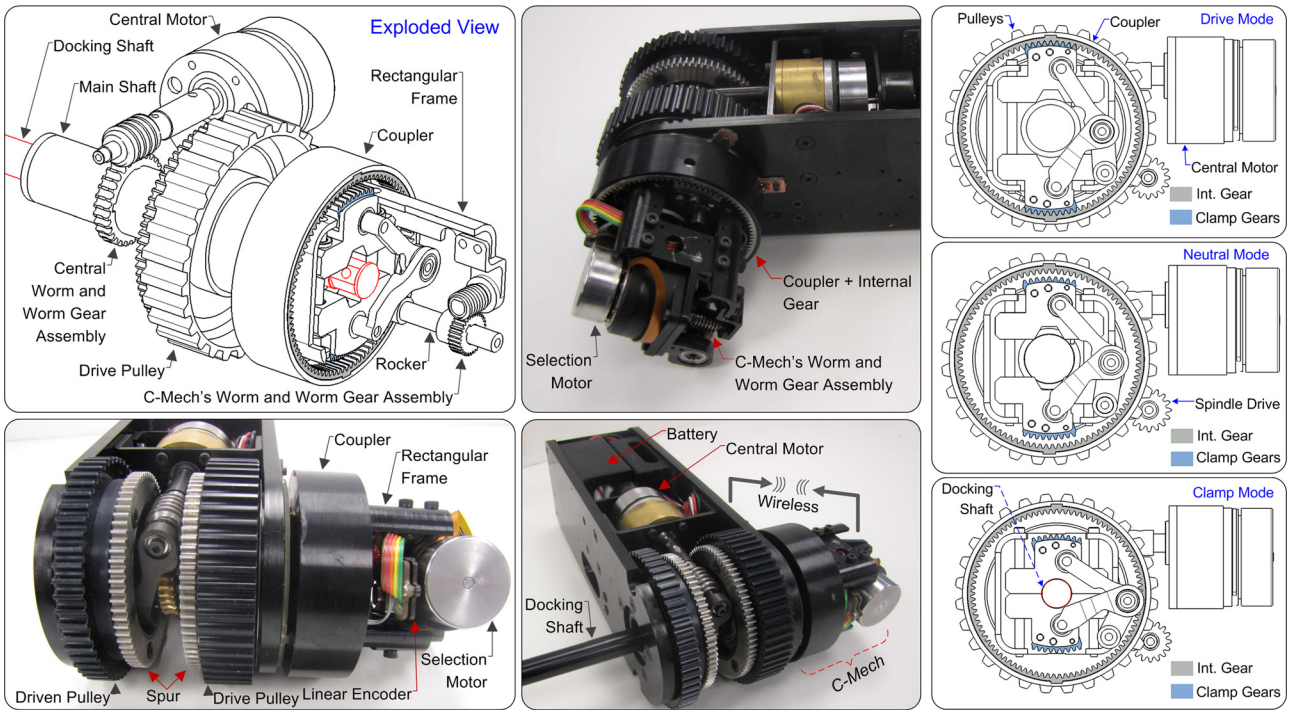

Fig. 9 Exploded schematic view of the tristate docking interface, its three modes of operation, and a proof-of-concept prototype shown connected to a small mobile robot (Central Motor: 50 W, 35 N m max. torque, Selection Motor: 15 W, 12 N m max. torque)

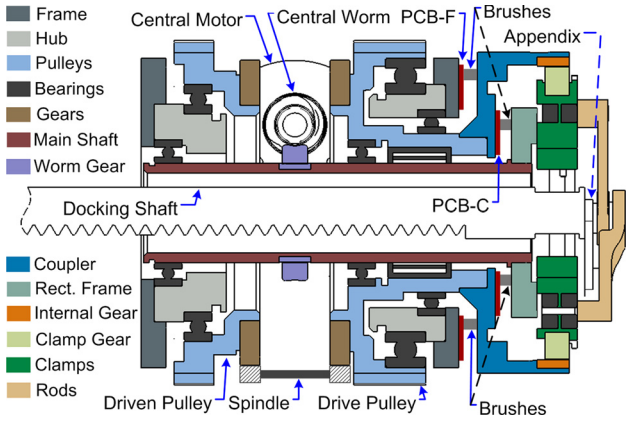

Fig. 10 Transmission schematic of the tristate docking interface

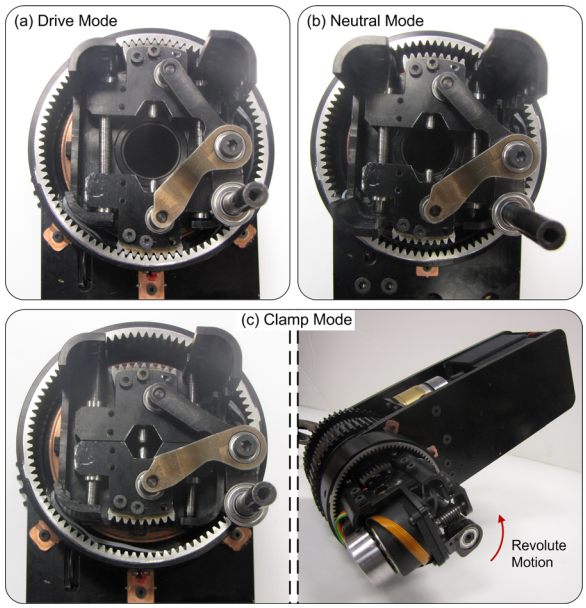

Fig. 11 Three modes of operation of the docking interface, and the active revolute joint in the clamp mode: (a) Drive Mode, (b) Neutral Mode, (c) Clamp mode

of the mechanism, which is reached simultaneously by the two sliders as a result of the optimal design presented in Sec. 3. This is further highlighted in Fig. 12, where linear encoder measurements of the combined ascending stroke of the two sliders in the proof-of-concept prototype (Figs. 9 and 11) are shown to closely match the simulation results of the case-study optimality analysis provided in Sec. 5.2.

When this gear engagement occurs, the central motor torque, transmitted to the *C-Mech* via the central worm and worm gear assembly, will be redirected toward the coupler. This coupler's rotation is transmitted directly to the driving system of the module, such as a pulley, since the two are rigidly connected together (Fig. 10). This provides mobility for the module via the central motor.

6.2.2 Neutral Mode. In the *neutral mode* (Figs. 10 and 11(*b*)), the sliders are positioned along the intermediate stroke to disengage the internal gear, causing the *C-Mech* to rotate idly inside the coupler. This idle rotation enables the orientation of the clamps' pins to the docking shaft's interference holes prior to coupling. The relative displacement offset between the two sliders in the intermediate stroke is practically insignificant in this case, since the clamps do not interact with any elements of the interface in the *neutral mode*.

6.2.3 Clamp Mode. In the *clamp mode* (Figs. 10 and 11(*c*)), the sliders are driven down toward the central plane which represents the *close* boundary condition for the dual-rod mechanism. Here again, the optimal design of the dual-rod mechanism enables

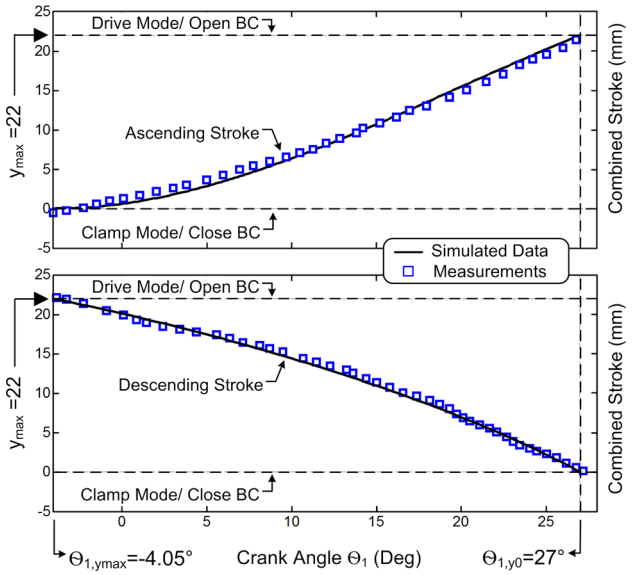

Fig. 12 Comparison of experimental and simulated optimal displacement of the two sliders of the dual-rod mechanism in the ascending and descending strokes. Note the conformity of the two datasets, and the ability of the two sliders to simultaneously reach the terminal boundary conditions in both cases (i.e., *e* = *0* at both Open *BC* and Close *BC*).

the two sliders to simultaneously reach the *clamp mode* in the descending stroke, as further highlighted experimentally in Fig. 12. This simultaneous interception enables the clamps' combined hexagonal aperture to mate with the neck of the docking shaft, where the latter will be inserted by an adjacent module inside the main hollow shaft of the module carrying the *C-Mech* (refer to the video animation in Ref. [33]).

When mating between the pins and the interference holes is established, a planetary motion is created around the docking shaft, where the latter is held stationary by the adjacent module. This mating converts the rotation of the central motor to a revolution of the module around this shaft which creates an active joint for this motion. This mode, along with the *drive* and *neural* modes, is demonstrated experimentally in the video file provided in Ref. [34].

We also note that the length l_1, the position c, and angle θ_{1,y_0} of the rocker are chosen in a way to ensure that the rocker's tip remains contained inside the coupler's circumference in order to avoid interference with the ground in this mode.

6.3 Comparison With Other Embodiments. The advantage of the dual-rod slider rocker mechanism over other non-back-drivable translational mechanisms, such as the leadscrew, lies in its small projected footprint. This difference is visualized in the comparison depicted in Fig. 13.

In this figure, it is shown that the width of the *C-Mech* implemented with the leadscrew adds ∼48% to the width of the *C-Mech* configured with the dual-rod mechanism (for a rod length of 24 mm, the length of the nut stroke on the leadscrew is 21 mm for y_{max} = 11mm). This increase in width does not account for the size of the second gear stage established by the worm and worm gear assembly in the case of the dual-rod system. Indeed, if this stage is added to the leadscrew option, the width of *C-Mech* nearly doubles, making the interface impractical for modular robotics.

We note that in Fig. 13, the selection motor was placed in series with the leadscrew in order to ensure that the *C-Mech* assembly remains contained inside the circumference of the coupler. This constraint is satisfied by the dual-rod system, where the motor occupies the coupler's lateral diametral space, and thus it should also be satisfied by any other mechanism in order to provide common bases for comparison. A summary of additional embodiments for the torque recirculation scheme is provided in Table 2.

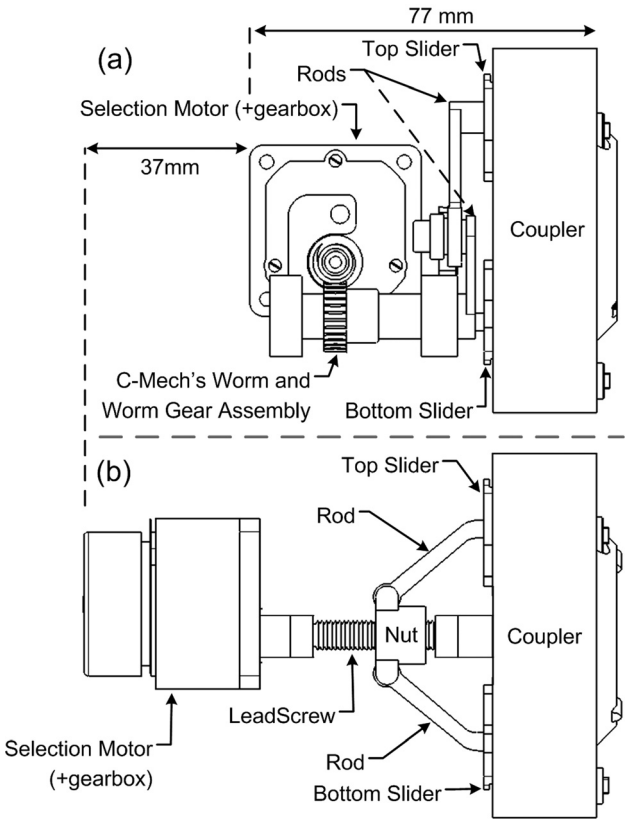

Fig. 13 Width comparison of the *C-Mech* with (*a*) dual-rod slider rocker mechanism and (*b*) lead screw mechanism

Table 2 Additional possible embodiments

Mechanism	Shortcoming
Cam-follower	Violates the non-back-drivability constraint due to the rolling contact between the cam and the follower
Linear actuator	Provides low actuation torque relative to its size. Implementation may dictate two actuators to drive both sliders independently

6.4 Structural Non-Back-Drivability: Role of the Pins. In addition to the mechanical non-back-drivability of the docking interface provided by the *C-Mech*'s worm and worm gear assembly, the protruded pins play a significant role in reinforcing the *clamp mode*. This role is evident in the amplification of the yield torque up to a threshold that satisfies the rigidity requirements of an active joint for modular robotic applications with manipulation. Herein, we define the yield torque as the maximum torque applied to the active joint in the *clamp mode* at which a relative slip between the docking shaft and the clamps occurs. This slip is due to the separation of the clamps under excessive loading.

A finite element analysis of the dual-rod slider rocker mechanism—shown earlier in the docking interface of Figs. 9 and 11—highlights the role of the pins in this process. This analysis is performed as an assembly, where an anchor boundary condition is applied to the rocker (in the *clamp mode*, the rocker is stationary). Contact constraints are subsequently applied to simulate the physical interaction between the different components of the actual

mechanism in a way to make the entire assembly stationary relative to the anchor.

Two comparative simulations are performed on this model as illustrated in Fig. 14. In Fig. 14(*a*), the pins were removed from the clamps, and a contact constraint was defined between the hexagonal faces of the docking shaft and those of the combined hexagonal aperture of the clamps. The subsequent simulation shows that separation occurs, despite the stationarity of the rocker, where the gap separating the two clamps increases as a function of the incremental torque applied to the docking shaft as illustrated in Fig. 15(*a*).

This separation is due to the force component that the torque acting on the docking shaft induces along the rails of the mechanism. Such component forces the rocker to bend elastically, and yield a separation gap λ which can be written in terms of the docking shaft's rotation angle φ as

$$\lambda = D\left(1 - \frac{\cos(\varphi) + \cos(60 - \varphi)}{2}\right) - \frac{D}{2}(\mathrm{sgn}(30 - \varphi))\sin(30 - \varphi) \tag{26}$$

where D denotes the diameter of the circumcircle of the docking shaft's hexagonal neck, and sgn the sign function. Thus, for the docking shaft of the prototyped interface with a diameter $D = 12$mm, separation occurs at a gap $\lambda = 1.6$mm according to (26), as further validated in the simulation results plotted in Fig. 15(*a*) at a yield torque of 24 N m.

However, when the pins are introduced as shown in Fig. 14(*b*), the force component along the rails is eliminated. This is due to the action/reaction interaction between the pins and the interference holes, where the rotation of the docking shaft that initiates this force component along the rails is resisted by the pins, thus preventing such component from happening. As a result, the clamps cannot displace along the rails, and are rather twisted together as a rigid body under torsional loading.

More importantly however, the pins prevent the propagation of the input torque from the docking shaft toward the rocker, and ultimately toward the selection motor which drives the rocker through the *C-Mech*'s worm and worm gear assembly. This behavior is visualized in Fig. 15(*b*), where the twist of the clamps—as a rigid body—propagates the stress toward the rails instead of the rocker. Because the rocker is shielded in this process, a minimal static torque will be required at the worm and

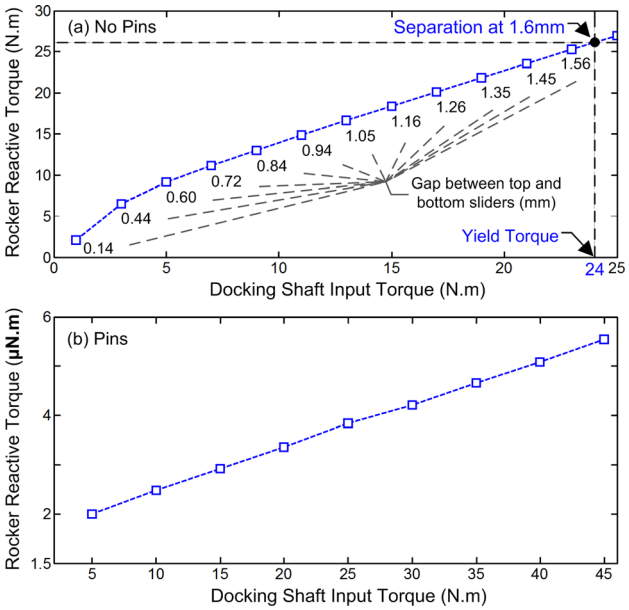

Fig. 15 Rocker torque as a function of the torque applied on the active joint in the *clamp mode*. (*a*) No pins, note the separation at 24 N m, (*b*) with pins.

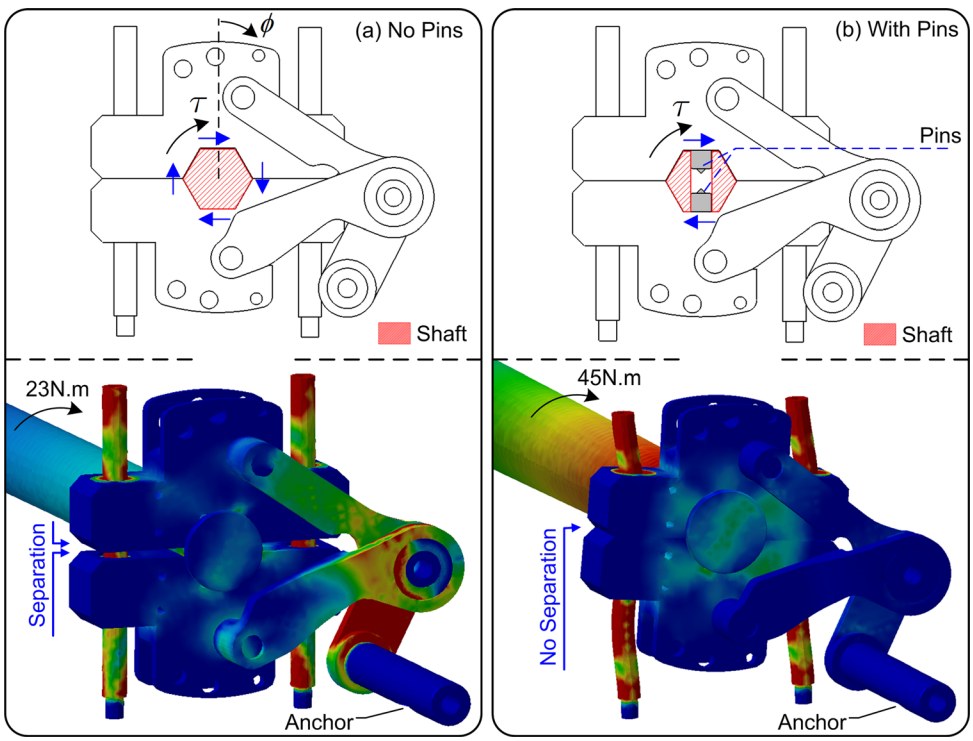

Fig. 14 Finite elements analysis of the dual-rod slider rocker mechanism in the *clamp mode*. (*a*) Clamp separation gap at a torque of 23 N m without pins. (*b*) No separation with pins, and load propagation toward the rails (input torque 45 N m).

worm gear assembly to maintain the non-back-drivability of the mechanism, thus making the yield torque of the interface a structural consideration that depends on the dimensions of the rails. This property is further visualized in Fig. 15(*b*), which shows a near zero ideal static torque at the rocker for an incremental input torque up to 45 N m.

7 Conclusion

This paper presented an optimal design and dynamic analysis of a new mechanism called the *dual-rod slider rocker mechanism*. This mechanism enables the translation of two sliders via a single rocker (motor), and is thus characterized by a small projected footprint which broadens its industrial utility to applications where size and weight are a critical design constraint, such as space and mobile robotics. A sample application was reported in this paper, where the mechanism was integrated in a docking interface for modular robotics, as part of a torque recirculation scheme that enables three independent modes of operation via a single motor. A proof-of-concept prototype was developed, and a finite element analysis was performed to demonstrate the ability of the dual-rod mechanism to provide a high yield torque at the active joint created by this interface in the *clamp mode*.

Such results represent the basis for our future investigations, where we further integrate the dual-rod mechanism and test the rigidity of the ensuing tristate coupling interface on a modular robotic system for rough terrain mobility and manipulation, such as STORM [33].

Acknowledgment

The authors wish to thank Zhou Ma and Eric Alvarez for their contribution to the prototype of the docking interface.

Nomenclature (in reference to Fig. 2)

X_0Y_0 = global Cartesian frame

l_1, l_2, l_2' = length of the rocker, the top rod, and the bottom rod, respectively

$\theta_1, \theta_2, \theta_2'$ = rocker angle, top rod angle, and bottom rod angle relative to the Y_0-axis, respectively

$\theta_{1,y_0}, \theta_{1,y_{max}}$ = rocker angle at $y = 0$ and $y = y_{max}$, respectively

b, b' = distance between Y_0-axis and the top and bottom rod/slider joint axis along X_0-axis, respectively

h = distance between the top rod/slider joint axis and the bottom edge of the top slider, along Y_0-axis

h' = distance between the bottom rod/slider joint axis and the top edge of the bottom slider, along Y_0-axis

c = distance between X_0-axis and the central plane, measured along Y_0-axis

y, y' = distance between bottom (top) edge of top (bottom) slider and the central plane, measured along Y_0-axis

y_{max} = stroke length of each slider, also defined as the position of the *open* terminal boundary condition

M_1 = mass of the rocker

M_2, M_2' = mass of the top and bottom rods, respectively

M_3, M_3' = mass of the top and bottom sliders, respectively

References

[1] Smith, J. E., Smith, J. C., and McKisic, A. D., 1991, "A Comparative Study of the Stiller-Smith and Slider-Crank Mechanisms for Eight-Cylinder Internal Combustion Engine Use," ASME J. Eng. Gas Turbines Power, **113**, pp. 350–358.

[2] Liniecki, A., 1970, "Synthesis of a Slider-Crank Mechanism With Consideration of Dynamic Effects," J. Mech., **5**(3), pp. 337–349.

[3] Lieh, J., 1994, "Dynamic Modeling of a Slider-Crank Mechanism With Coupler and Joint Flexibility," Mech. Mach. Theory, **29**(1), pp. 139–147.

[4] Zhang, W. J., and Li, Q., 2006, "A Closed-Form Solution to the Crank Position Corresponding to the Maximum Velocity of the Slider in a Centric Slider-Crank Mechanism," ASME J. Mech. Des., **128**, 654–656.

[5] Figliolini, G., Conte, M., and Rea, P., 2012, "Algebraic Algorithm for the Kinematic Analysis of Slider-Crank/Rocker Mechanisms," ASME J. Mech. Rob., **4**(1), p. 011003.

[6] Soylemez, E., 2002, "Classical Transmission-Angle Problem for Slider-Crank Mechanisms, Mech. Mach. Theory, **37**(4), pp. 419–425.

[7] Russell, K., and Sodhi, S. R., 2005, "On the Design of Slider-Crank Mechanisms. Part I: Multi-Phase Motion Generation," Mech. Mach. Theory, **40**(3), pp. 285–299.

[8] Tanik, E., 2011, "Transmission Angle in Compliant Slider-Crank Mechanism," Mech. Mach. Theory, **46**(11), pp. 1623–1632.

[9] Myszka, D., and Murray, A., 2010, "Slider-Cranks as Compatibility Linkages for Parametrizing Center-Point Curves," ASME J. Mech. Rob., **2**(2), p. 021007.

[10] Erkaya, S., Su, S., and Uzmay, I., 2007, "Dynamic Analysis of a Slider–Crank Mechanism With Eccentric Connector and Planetary Gears," Mech. Mach. Theory, **42**(4), pp. 393–408.

[11] Yi-Ming, W., 2005, "The Dynamics of a Slider-Crank Mechanism With an Initially Curved Coupler Under Two-Component Parametric Resonance," J. Sound Vib., **280**(3–5), pp. 815–835.

[12] Fung, R.-F., 1996, "Dynamic Analysis of the Flexible Connecting Rod of a Slider-Crank Mechanism," ASME J. Vibr. Acoust., **118**, pp. 687–689.

[13] Fallahi, B., Lai, S., and Venkat, C., 1995, "A Finite Element Formulation of a Flexible Slider Crank Mechanism Using Local Coordinates," ASME J. Dyn. Syst., Meas., Control, **117**, pp. 329–334.

[14] Tadjbakhsh, I., and Younis, C., 1986, "Dynamic Stability of the Flexible Connecting Rod of a Slider Crank Mechanism," ASME J. Mech., Transm., Autom. Des. **108**, pp. 487–496.

[15] Khemili, I., and Romdhane, L., 2008, "Dynamic Analysis of a Flexible Slider–Crank Mechanism With Clearance," Eur. J. Mech. A/Solids, **27**(5), pp. 882–898.

[16] Antonescu, P., and Udriste, P. C., 1973, "Synthesis of Spatial Slider-Crank Mechanism for Given Slider Stroke and Crank Length," Mech. Mach. Theory, **8**(2), pp. 257–269.

[17] Premkumar, P., Dhall, S. R., and Kramer, S. N., 1988, "Selective Precision Synthesis of the Spatial Slider Crank Mechanism for Path and Function Generation," J. Mech. Trans., **110**, pp. 295–302.

[18] Parlaktas, V., and Tanik, E., 2011, "Partially Compliant Spatial Slider–Crank (RSSP) Mechanism," Mech. Mach. Theory, **46**(11), pp. 1707–1718.

[19] Shoup, T. E., 1984, "The Design of an Adjustable, Three Dimensional Slider Crank Mechanism," Mech. Mach. Theory, **19**(1), pp. 107–111.

[20] Yan, H.-S., and Liu, J.-Y., 1993, "Geometric Design and Machining of Variable Pitch Lead Screws With Cylindrical Meshing Elements," ASME J. Mech. Des. **115**, pp. 490–495.

[21] Hollander, K., and Sugar, T. G., 2008, "Design of Lightweight Lead Screw Actuators for Wearable Robotic Applications," ASME J. Mech. Des., **128**, pp. 644–648.

[22] Yim, M., Shen, W.-M., Salemi, B., Rus, D., Moll, M., Lipson, H., Klavins, E., and Chirikjian, G. S., 2007, "Modular Self-Reconfigurable Robot Systems: Challenges and Opportunities for the Future," IEEE Rob. Autom. Mag., **14**(1), pp. 2–11.

[23] Moubarak, P., and Ben-Tzvi, P., 2012, "Modular Reconfigurable Mobile Robotics," Rob. Auton. Syst., **60**(12), pp. 1648–1663.

[24] Sao, T., Song, Y., Li, Y., and Zhang, J., 2010, "Workspace Decomposition Based Dimensional Synthesis of a Novel Hybrid Reconfigurable Robot," ASME J. Mech. Rob., **2**(3), p. 031009.

[25] Liu, G. P., Yang, J. B., and Whidborne, J. F., 2002, *Multiobjective Optimisation and Control*, 1st ed., Research Studies Press, Baldock, Hertfordshire, England, Chap. 1, p. 4.

[26] Liu, M., Cao, Y., Zhang, Q., and Zhou, H., 2010, "Kinematics and Dynamics Simulation of the Slider-Crank Mechanism Based on Matlab/Simulink," International Conference on Computer Application and System Modeling (ICCASM'10), Taiyuan, China.

[27] Østergaard, E. H., and Kassow, K., 2006, "Design of the ATRON Lattice-Based Self-Reconfigurable Robot," Auton. Rob., **21**(2), pp. 165–183.

[28] Zykov, V., Mytilinaois, E., Desnoyer, M., and Lipson, H., 2007, "Evolved and Designed Self-Reproducing Modular Robotics," IEEE Trans. Rob., **23**(2), pp. 308–319.

[29] Park, M., Chitta, S., Teichman, A., and Yim, M., 2008, "Automatic Configuration Recognition Methods in Modular Robots," Int. J. Robot. Res., **27**(3–4), pp. 403–421.

[30] Yim, M., Zhang, Y., Roufas, K., Duff, D., and Eldershaw, C., 2002, "Connecting and Disconnecting for Chain Self-Reconfiguration With PolyBot," IEEE/ASME Trans. Mechatron., **7**(4), pp. 442–451.

[31] Ünsal, C., Kiliççöte, H., and Khosla, P. K., 2001, "A 3-D Modular Self-Reconfigurable Bipartite Robotic System: Implementation and Motion Planning," Auton. Rob., **10**(1), pp. 23–40.

[32] Brown, H. B., Vande Weghe, J. M., Bererton, C. A., and Khosla, P. K., 2002, "Millibot Train for Enhanced Mobility," IEEE/ASME Trans. Mechatron., **7**(4), pp. 452–461.

[33] Moubarak, P., and Ben-Tzvi, P., 2011, "STORM Animation," retrieved on February 2011, http://www.seas.gwu.edu/∼bentzvi/STORM/STORM_VR_Animation.html

[34] Moubarak, P., Ben-Tzvi, P., Ma, Z., and Alvarez, E., 2012, "Demonstration of the Three Modes of Operation of the Tri-Partite Docking Interface," retrieved on January 2012, http://www.seas.gwu.edu/∼bentzvi/STORM/DOK.html